Engineering Solutions to Mechanics, Marine Structures and Infrastructures

Eng. Solut. Mech. Mar. Struct. Infrastruct.
2024.1(1).7
ISSN: 2960-0979
https://doi.org/10.58531/esmmsi/1/1/7

Article

Numerical Investigation into the Thermo-Hydro-Mechanical Behavior in Unsaturated Soils Considering Hypergravity Effect

Zhigang Ye[1, 2, 3], Chaofan Chen[4], Yingtao Hu[5], Zhangbo Wan[1, 2, 3], Dapeng Zhang[6], Ronghan Guo[1, 2, 3, *]

[1] MOE Key Laboratory of Soft Soils and Geoenvironmental Engineering, Zhejiang University, 310058, China
[2] College of Civil Engineering and Architecture, Zhejiang University, 310058, China
[3] Center for Hypergravity Experimental and Interdisciplinary Research, Zhejiang University, 310058, China
[4] Geotechnical Institute, Technische Universität Bergakademie Freiberg, 09599, Freiberg, Germany
[5] School of Engineering, Hangzhou City University, Hangzhou, Zhejiang, 310015, China
[6] Naval Architecture and Shipping College, Guangdong Ocean University, Zhanjiang, 524088, China
[*] Corresponding author: 22312025@zju.edu.cn

Academic Editor: Weiwei Wang < zhwangww@ytu.edu.cn>
Received: 24, February, 2024; Revised: 15, March, 2024; Accepted: 18, March, 22024; Published: 18, March, 2024

Abstract: Unsaturated soils are commonly found in coastal regions and marine sediments, where understanding the thermo-hydro-mechanical (THM) behavior, especially regarding phase transition, is crucial for related practical engineering applications. Centrifugal model offers an effective means to reflect the prototype with smaller scale and shorter duration under hypergravity conditions. Present studies on similarity based on governing equation analysis of the THM coupled responses are mainly focused on saturated rather than unsaturated soils, nor involved with different boundary conditions. This paper theoretically derives the similarity of THM behavior of unsaturated soils between the centrifugal model and prototype, and numerically assesses the similarity considering Dirichlet / Neumann condition based on the open-source FEM code OpenGeoSys. In addition, numerical results shows that phase transition between liquid water and water vapor will occur under temperature variation, and pore pressure difference rather than initial pore pressure causes the difference of THM coupled responses. Significant pore pressure variation will be amplified with increase of gas diffusion coefficient, and large air entry pressure corresponds to high liquid saturation and obvious phase transition.

Citation: Ye Z., Chen C., Hu Y., Wan Z., Zhang D., Guo R. Numerical Investigation into the Thermo-Hydro-Mechanical Behavior in Unsaturated Soils Considering Hypergravity Effect. Eng. Solut. Mech. Mar. Struct. Infrastruct., 2024, 1(1), doi: 10.58531/esmmsi/1/1/7

Keywords: Unsaturated soils; Thermo-hydro-mechanical coupled; phase transition; Similarity of centrifugal model; OpenGeoSys.

1. Introduction

Coastal regions and marine sediments typically exist in an unsaturated state due to atmospheric intrusion or generated gas from biogenetic or pyrolysis processes. Practical engineering endeavours are often associated with unsaturated soils, encompassing gas hydrate exploitation [1, 2], heated pipes for waxy or high viscosity oil [3, 4], energy piles [5], and highway or airfield pavements [6]. In these scenarios, the impacts of temperature variation are significant and cannot be disregarded, influencing both heat transfer within the engineering structures and environmentally driven diurnal/seasonal cycles. Specifically, thermal fluctuations induce liquid / gas expansion in soil pores, resulting in changes in pore liquid / gas pressure. Accumulation and dissipation of pore pressure, in return, affect soil stresses, influencing liquid-gas migration and heat transfer. Besides, phase transition, including liquid water evaporation and water vapor condensation, can be triggered by temperature or pore pressure variations. These intricate processes belong to the thermo-hydro-mechanical (THM) coupled behavior in unsaturated soils, a complexity further compounded by the gravity.

In the realm of these engineering applications, 1g-models [7] and centrifugal models [8] proves to be an effective approach for studying THM problems, offering a balance between short duration and cost-effectiveness. Theoretical foundations for these tests rely on scaling laws, including dimensional analysis [9] and governing equation analysis [10]. According to these theories, 1g-models are generally suitable for a broad range of scenarios, whereas centrifugal models are particularly valuable for situations closely tied to gravity effects, especially in the context of soil consolidations and stress-related processes. Ng et al. [8] investigated the effects of cyclic heating and cooling on the long-term displacement of energy piles in a centrifuge with both lightly over-consolidated and heavily over-consolidated kaolin clay. Stewart and McCartney [11] carried out a centrifuge test to characterize the transient thermomechanical response of energy foundations during heating-cooling cycles. Through integrating theory derivation and numerical modelling, it becomes possible to assess the similarity between the prototype and centrifugal model in THM coupled processes in unsaturated soils. This approach allows for a comprehensive evaluation of the impact of gravity on these processes.

Earlier investigations into similarity, particularly through governing equation analysis, have predominantly concentrated on saturated soils, with limited exploration in the realm of unsaturated soils, which pose greater complexity. The detailed examination of similarity has primarily focused on parameters, neglecting a thorough consideration of boundary conditions that can vary significantly depending on specific problems. In addition, phase transition, a common occurrence in unsaturated soils, introduces further complexities, and the extent to which conditions and parameters influence THM coupled responses remains largely unknown. In response to this gap in understanding, theoretical derivations regarding THM coupled behavior have been conducted in unsaturated soils, encompassing both parameter and boundary conditions. The associated numerical simulations exploring similarity have

been executed using a THM coupled model based on the open-source FEM solver OpenGeoSys [12, 13]. To delve deeper into the intricacies of these systems, a final step involves a parametric analysis of conditions (*e.g.*, temperature variation and initial pore pressure) and typical parameters (*e.g.*, gas diffusion coefficient and air entry pressure), aiming to unravel their respective impacts on THM coupled behavior.

2. Methodology

2.1 Governing Equations

The THM coupled processes in unsaturated soils primarily involve heat transfer (**T**), liquid-gas migration (**H2)**, and skeleton deformation (**M**), as shown in Figure. 1. Within **H2**, phase transition, encompassing liquid water evaporation and water vapor condensation, is a representation process. **H2** will influence **T** and **M** respectively through heat advection and effective stresses. **T** plays a crucial role in phase transition and thermal strains/stresses, while **M** causes strain energy and pore pressure variations. Thus, liquid pressure p^{l}, gas pressure p^{g} temperature T, and displacements **u** are treated as independent variables, leading to the governing equations described below.

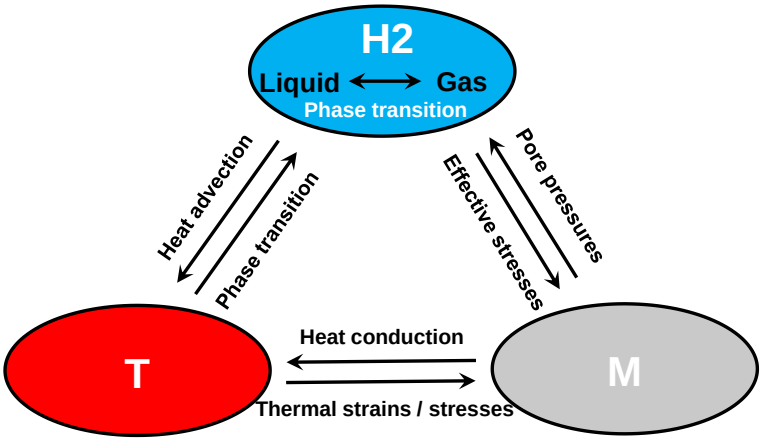

Figure. 1. THM coupled processes of unsaturated soils.

2.1.1 Mass balance equation

Mass equation referred to pore air and water components can be expressed as [14]:

$$\frac{\mathrm{d_s}}{\mathrm{d}t}\left(\rho_{\mathrm{a}}^{\mathrm{g}} S^{\mathrm{g}} \varphi\right)+\nabla\cdot\left(\mathbf{J}_{\mathrm{a}}^{\mathrm{g}}\right)+\rho_{\mathrm{a}}^{\mathrm{g}} S^{\mathrm{g}} \varphi \nabla\cdot\frac{\mathrm{d_s}\mathbf{u}}{\mathrm{d}t}=q_{\mathrm{a}} \tag{1a}$$

$$\frac{\mathrm{d_s}}{\mathrm{d}t}\left(\rho_{\mathrm{w}}^{\mathrm{l}} S^{\mathrm{l}} \varphi+\rho_{\mathrm{w}}^{\mathrm{g}} S^{\mathrm{g}} \varphi\right)+\nabla\cdot\left(\mathbf{J}_{\mathrm{w}}^{\mathrm{l}}+\mathbf{J}_{\mathrm{w}}^{\mathrm{g}}\right)+\left(\rho_{\mathrm{w}}^{\mathrm{l}} S^{\mathrm{l}} \varphi+\rho_{\mathrm{w}}^{\mathrm{g}} S^{\mathrm{g}} \varphi\right)\nabla\cdot\frac{\mathrm{d_s}\mathbf{u}}{\mathrm{d}t}=q_{\mathrm{w}} \tag{1b}$$

where $\frac{\mathrm{d_s}}{\mathrm{d}t}$ = material time derivative following the solid skeleton, ∇ = Nabla operator, $\rho_{\mathrm{a}}^{\mathrm{g}}$, $\rho_{\mathrm{w}}^{\mathrm{l}}$ and $\rho_{\mathrm{w}}^{\mathrm{g}}$ = density of dry air, liquid water and water vapor, respectively, S^{g} and S^{l} = saturation of gas and liquid phase, φ = porosity, $\mathbf{J}_{\mathrm{a}}^{\mathrm{g}}$, $\mathbf{J}_{\mathrm{w}}^{\mathrm{l}}$ and $\mathbf{J}_{\mathrm{w}}^{\mathrm{g}}$ = flux of dry air, liquid water and water vapor, **u** = displacements, and q_{a} and q_{w} = source term of air and water,

respectively, which equals to zero here. $\mathbf{J}_{\alpha\mathrm{C}}^{\mathrm{g}}$ and $\mathbf{J}_{\alpha\mathrm{D}}^{\mathrm{g}}$ = flux of advective part and diffusive part for α, where α = component of pore air / water vapor. $\mathbf{J}_{\mathrm{w}}^{\mathrm{l}}$ and $\mathbf{J}_{\alpha\mathrm{C}}^{\mathrm{g}}$ follows Darcy's law and $\mathbf{J}_{\alpha\mathrm{D}}^{\mathrm{g}}$ obeys Fick's law respectively:

$$\mathbf{J}_{\mathrm{w}}^{\mathrm{l}} = -\frac{\rho_{\mathrm{w}}^{\mathrm{l}}\mathbf{K}k^{\mathrm{l}}}{\mu^{\mathrm{l}}}\left(\nabla p^{\mathrm{l}} - \rho_{\mathrm{w}}^{\mathrm{l}}\mathbf{g}\right) \tag{2a}$$

$$\mathbf{J}_{\alpha\mathrm{C}}^{\mathrm{g}} = -\frac{\rho_{\alpha}^{\mathrm{g}}\mathbf{K}k^{\mathrm{g}}}{\mu^{\mathrm{g}}}\left(\nabla p^{\mathrm{g}} - \rho^{\mathrm{g}}\mathbf{g}\right) \quad \alpha=\mathrm{a},\ \mathrm{w} \tag{2b}$$

$$\mathbf{J}_{\alpha\mathrm{D}}^{\mathrm{g}} = -\rho^{\mathrm{g}}\frac{M_{\mathrm{a}}M_{\mathrm{w}}}{\left(M_{\mathrm{g}}\right)^{2}}\mathbf{D}_{\mathrm{a}}\nabla\left(\frac{p_{\alpha}^{\mathrm{g}}}{p^{\mathrm{g}}}\right) \quad \alpha=\mathrm{a},\ \mathrm{w} \tag{2c}$$

where $\mathbf{K}$ = permeability, k^{g} and k^{l} = relative permeability coefficient of gas and liquid phase, μ^{g} and μ^{l} = viscosity of gas and liquid phase, $\mathbf{g}$ = gravity constant, M_{a} and M_{w} = molar masses of dry air and water, $\mathbf{D}_{\mathrm{a}}$ = diffusion coefficient of dry air, and $p_{\mathrm{a}}^{\mathrm{g}}$ = dry air partial pressure. ρ^{g} and M_{g} = density and molar mass of the mixture gas containing dry air and vapor.

2.1.2 Energy conservation equation

The energy conservation equation for all phases is as follows [14]:

$$(\rho C)\frac{\mathrm{d}_{\mathrm{s}}T}{\mathrm{d}t} + \nabla\cdot\mathbf{J}_{\mathrm{c}} + \nabla\cdot\left(\mathbf{J}_{\mathrm{E}}^{\mathrm{l}} + \mathbf{J}_{\mathrm{E}}^{\mathrm{g}}\right) = q_{\mathrm{E}} \tag{3}$$

where $\mathbf{J}_{\mathrm{c}}$ = heat conduction flux, $\mathbf{J}_{\mathrm{E}}^{\mathrm{l}}$ and $\mathbf{J}_{\mathrm{E}}^{\mathrm{g}}$ = heat advection flux respectively caused by liquid and gas flow, q_{E} = energy source term, equaling to zero, and ρC = equivalent mass heat capacity, calculated by $\rho C = C^{\mathrm{s}}\rho^{\mathrm{s}}(1-\varphi) + C^{\mathrm{l}}\rho^{\mathrm{l}}S^{\mathrm{l}}\varphi + C^{\mathrm{g}}\rho^{\mathrm{g}}S^{\mathrm{g}}\varphi$.

The heat transfer includes conduction and advection, and the former one is usually described by Fourier's law and the later ones are related to fluid velocity:

$$\mathbf{J}_{\mathrm{c}} = -\mathbf{k}_{T}\nabla T \tag{4a}$$

$$\mathbf{J}_{\mathrm{E}}^{\mathrm{l}} = C^{\mathrm{l}}\rho^{\mathrm{l}}\mathbf{v}^{\mathrm{l}}T \tag{4b}$$

$$\mathbf{J}_{\mathrm{E}}^{\mathrm{g}} = C^{\mathrm{g}}\rho^{\mathrm{g}}\mathbf{v}^{\mathrm{g}}T \tag{4c}$$

where C^{s}, C^{l} and C^{g} = specific heat capacity of soil, liquid and gas, respectively, $\mathbf{v}^{\mathrm{l}}$ and $\mathbf{v}^{\mathrm{g}}$ = seepage velocity of liquid and gas, ρ^{s} = soil density, and $\mathbf{k}_{T}$ = equivalent heat conductive coefficient, formulated as $\mathbf{k}_{T} = \mathbf{k}^{\mathrm{s}}(1-\varphi) + \mathbf{k}^{\mathrm{l}}S^{\mathrm{l}}\varphi + \mathbf{k}^{\mathrm{g}}S^{\mathrm{g}}\varphi$.

2.1.3 Linear momentum balance equation

Neglecting inertial forces, the mechanical equilibrium equation is governed by [14]:

$$\nabla\cdot\left(\boldsymbol{\sigma}' - \left(S^{\mathrm{l}}p^{\mathrm{l}} + S^{\mathrm{g}}p^{\mathrm{g}}\right)\mathbf{1}\right) + \rho\mathbf{g} = \mathbf{0} \tag{5}$$

where $\mathbf{1}$ = second-order identity tensor, ρ = equivalent density of all phases, calculated by $\rho = \rho^{\mathrm{s}}(1-\varphi)+\rho^{\mathrm{l}}S^{\mathrm{l}}\varphi+\rho^{\mathrm{g}}S^{\mathrm{g}}\varphi$, and $\boldsymbol{\sigma}'$ = effective stress tensor, which can be expressed by linear elasticity relationship:

$$\boldsymbol{\sigma}' = \mathbf{D}^{\mathbf{e}}:(\boldsymbol{\varepsilon}-\boldsymbol{\varepsilon}_T) = \mathbf{D}^{\mathbf{e}}:\frac{\nabla\mathbf{u}+\nabla^{\mathrm{T}}\mathbf{u}}{2} - \mathbf{D}^{\mathbf{e}}:\mathbf{1}\frac{\beta_{\mathrm{s}}}{3}(T-\mathrm{T}_0) \tag{6}$$

where $\mathbf{D}^{\mathbf{e}}$ = elasticity tensor, $\boldsymbol{\varepsilon}$ = total strain tensor, $\boldsymbol{\varepsilon}_T$ = thermal strain tensor, β_{s} = volumetric thermal expansion coefficient of solid phase, T_0 = initial temperature.

2.2 Scaling laws for centrifugal model

2.2.1 Governing equations

Centrifugal model tests offer a convenient and cost-effective means of reflecting practical engineering scenarios. Consequently, determining scale factors for parameters is crucial, and this is often achieved through the application of scaling laws. The fundamental dimensionless parameters for sizes and stresses include:

$$l_{\mathrm{r}}=\frac{l_{\mathrm{m}}}{l_{\mathrm{p}}}=\frac{1}{N} \tag{7a}$$

$$\sigma_{\mathrm{r}}=\frac{\sigma_{\mathrm{m}}}{\sigma_{\mathrm{p}}}=\frac{\rho_{\mathrm{m}}g_{\mathrm{m}}h_{\mathrm{m}}}{\rho_{\mathrm{p}}g_{\mathrm{p}}h_{\mathrm{p}}}=1 \tag{7b}$$

where the subscript m, p and r separately represent parameters of the model, the prototype and the scale factor, l is the length, h is the height along the direction of gravity, and σ is the scalar form of $\boldsymbol{\sigma}$. Thus, we obtain the scale factor for gravity acceleration, N:

$$g_{\mathrm{r}}=\frac{g_{\mathrm{m}}}{g_{\mathrm{p}}}=N \tag{8}$$

The mass balance equations of both the centrifugal model and the prototype for air and water are as follows:

$$\frac{\mathrm{d}_{\mathrm{s}}}{\mathrm{d}t_{\mathrm{m}}}\left(\rho^{\mathrm{g}}_{\mathrm{am}}S^{\mathrm{g}}_{\mathrm{m}}\varphi_{\mathrm{m}}\right)+\nabla\cdot\left(\mathbf{J}^{\mathrm{g}}_{\mathrm{am}}\right)+\rho^{\mathrm{g}}_{\mathrm{am}}S^{\mathrm{g}}_{\mathrm{m}}\varphi_{\mathrm{m}}\nabla_{\mathrm{m}}\cdot\frac{\mathrm{d}_{\mathrm{s}}\mathbf{u}_{\mathrm{m}}}{\mathrm{d}t_{\mathrm{m}}}=0 \tag{9a}$$

$$\frac{\mathrm{d}_{\mathrm{s}}}{\mathrm{d}t_{\mathrm{p}}}\left(\rho^{\mathrm{g}}_{\mathrm{ap}}S^{\mathrm{g}}_{\mathrm{p}}\varphi_{\mathrm{p}}\right)+\nabla\cdot\left(\mathbf{J}^{\mathrm{g}}_{\mathrm{ap}}\right)+\rho^{\mathrm{g}}_{\mathrm{ap}}S^{\mathrm{g}}_{\mathrm{p}}\varphi_{\mathrm{p}}\nabla_{\mathrm{p}}\cdot\frac{\mathrm{d}_{\mathrm{s}}\mathbf{u}_{\mathrm{p}}}{\mathrm{d}t_{\mathrm{p}}}=0 \tag{9b}$$

$$\frac{\mathrm{d}_{\mathrm{s}}}{\mathrm{d}t_{\mathrm{m}}}\left(\rho^{\mathrm{l}}_{\mathrm{wm}}S^{\mathrm{l}}_{\mathrm{m}}\varphi_{\mathrm{m}}+\rho^{\mathrm{g}}_{\mathrm{wm}}S^{\mathrm{g}}_{\mathrm{m}}\varphi_{\mathrm{m}}\right)+\nabla\cdot\left(\mathbf{J}^{\mathrm{l}}_{\mathrm{wm}}+\mathbf{J}^{\mathrm{g}}_{\mathrm{wm}}\right)+\left(\rho^{\mathrm{l}}_{\mathrm{wm}}S^{\mathrm{l}}_{\mathrm{m}}\varphi_{\mathrm{m}}+\rho^{\mathrm{g}}_{\mathrm{wm}}S^{\mathrm{g}}_{\mathrm{m}}\varphi_{\mathrm{m}}\right)\nabla_{\mathrm{m}}\cdot\frac{\mathrm{d}_{\mathrm{s}}\mathbf{u}_{\mathrm{m}}}{\mathrm{d}t_{\mathrm{m}}}=0 \tag{9c}$$

$$\frac{\mathrm{d}_{\mathrm{s}}}{\mathrm{d}t_{\mathrm{p}}}\left(\rho^{\mathrm{l}}_{\mathrm{wp}}S^{\mathrm{l}}_{\mathrm{p}}\varphi_{\mathrm{p}}+\rho^{\mathrm{g}}_{\mathrm{wp}}S^{\mathrm{g}}_{\mathrm{p}}\varphi_{\mathrm{p}}\right)+\nabla\cdot\left(\mathbf{J}^{\mathrm{l}}_{\mathrm{wp}}+\mathbf{J}^{\mathrm{g}}_{\mathrm{wp}}\right)+\left(\rho^{\mathrm{l}}_{\mathrm{wp}}S^{\mathrm{l}}_{\mathrm{p}}\varphi_{\mathrm{p}}+\rho^{\mathrm{g}}_{\mathrm{wp}}S^{\mathrm{g}}_{\mathrm{p}}\varphi_{\mathrm{p}}\right)\nabla_{\mathrm{p}}\cdot\frac{\mathrm{d}_{\mathrm{s}}\mathbf{u}_{\mathrm{p}}}{\mathrm{d}t_{\mathrm{p}}}=0 \tag{9d}$$

When scaling laws is satisfied, there should exist:

$$\frac{\rho^{\mathrm{g}}_{\mathrm{ar}}S^{\mathrm{g}}_{\mathrm{r}}\varphi_{\mathrm{r}}}{t_{\mathrm{r}}}=\frac{\rho^{\mathrm{g}}_{\mathrm{ar}}K_{\mathrm{r}}k^{\mathrm{g}}_{\mathrm{r}}p^{\mathrm{g}}_{\mathrm{r}}}{l_{\mathrm{r}}\mu^{\mathrm{g}}_{\mathrm{r}}l_{\mathrm{r}}}=\frac{\rho^{\mathrm{g}}_{\mathrm{ar}}K_{\mathrm{r}}k^{\mathrm{g}}_{\mathrm{r}}\rho^{\mathrm{g}}_{\mathrm{r}}g_{\mathrm{r}}}{l_{\mathrm{r}}\mu^{\mathrm{g}}_{\mathrm{r}}}=\frac{\rho^{\mathrm{g}}_{\mathrm{r}}M_{\mathrm{ar}}M_{\mathrm{wr}}D_{\mathrm{r}}p^{\mathrm{g}}_{\mathrm{ar}}}{l_{\mathrm{r}}\left(M_{\mathrm{gr}}\right)^2l_{\mathrm{r}}p^{\mathrm{g}}_{\mathrm{r}}}=\frac{\rho^{\mathrm{g}}_{\mathrm{ar}}S^{\mathrm{g}}_{\mathrm{r}}\varphi_{\mathrm{r}}u_{\mathrm{r}}}{l_{\mathrm{r}}t_{\mathrm{r}}} \tag{10a}$$

$$\frac{\rho_{\mathrm{wr}}^{\mathrm{l}} S_{\mathrm{r}}^{\mathrm{l}} \varphi_{\mathrm{r}}}{t_{\mathrm{r}}} = \frac{\rho_{\mathrm{wr}}^{\mathrm{g}} S_{\mathrm{r}}^{\mathrm{g}} \varphi_{\mathrm{r}}}{t_{\mathrm{r}}} = \frac{\rho_{\mathrm{wr}}^{\mathrm{l}} K_{\mathrm{r}} k_{\mathrm{r}}^{\mathrm{l}} p_{\mathrm{r}}^{\mathrm{l}}}{l_{\mathrm{r}} \mu_{\mathrm{r}}^{\mathrm{l}} l_{\mathrm{r}}} = \frac{\rho_{\mathrm{wr}}^{\mathrm{l}} K_{\mathrm{r}} k_{\mathrm{r}}^{\mathrm{l}} \rho_{\mathrm{wr}}^{\mathrm{l}} g_{\mathrm{r}}}{l_{\mathrm{r}} \mu_{\mathrm{r}}^{\mathrm{l}}} = \frac{\rho_{\mathrm{wr}}^{\mathrm{g}} K_{\mathrm{r}} k_{\mathrm{r}}^{\mathrm{g}} p_{\mathrm{r}}^{\mathrm{g}}}{l_{\mathrm{r}} \mu_{\mathrm{r}}^{\mathrm{g}} l_{\mathrm{r}}} = \frac{\rho_{\mathrm{wr}}^{\mathrm{g}} K_{\mathrm{r}} k_{\mathrm{r}}^{\mathrm{g}} \rho_{\mathrm{r}}^{\mathrm{g}} g_{\mathrm{r}}}{l_{\mathrm{r}} \mu_{\mathrm{r}}^{\mathrm{g}}} = \frac{\rho_{\mathrm{r}}^{\mathrm{g}} M_{\mathrm{ar}} M_{\mathrm{wr}} D_{\mathrm{r}} p_{\mathrm{wr}}^{\mathrm{g}}}{l_{\mathrm{r}} (M_{\mathrm{gr}})^2 l_{\mathrm{r}} p_{\mathrm{r}}^{\mathrm{g}}} = \frac{\rho_{\mathrm{wr}}^{\mathrm{g}} S_{\mathrm{r}}^{\mathrm{g}} \varphi_{\mathrm{r}} u_{\mathrm{r}}}{l_{\mathrm{r}} t_{\mathrm{r}}} \quad (10b)$$

Similarly, the followings are derived from energy conservation and linear momentum balance equations:

$$\frac{(\rho C) T_{\mathrm{r}}}{t_{\mathrm{r}}} = \frac{k_{T\mathrm{r}} T_{\mathrm{r}}}{l_{\mathrm{r}} l_{\mathrm{r}}} = \frac{C_{\mathrm{r}}^{\mathrm{l}} \rho_{\mathrm{r}}^{\mathrm{l}} v_{\mathrm{r}}^{\mathrm{l}} T_{\mathrm{r}}}{l_{\mathrm{r}}} = \frac{C_{\mathrm{r}}^{\mathrm{g}} \rho_{\mathrm{r}}^{\mathrm{g}} v_{\mathrm{r}}^{\mathrm{g}} T_{\mathrm{r}}}{l_{\mathrm{r}}} \quad (11a)$$

$$\frac{\sigma'_{\mathrm{r}}}{l_{\mathrm{r}}} = \frac{S_{\mathrm{r}}^{\mathrm{l}} p_{\mathrm{r}}^{\mathrm{l}}}{l_{\mathrm{r}}} = \frac{S_{\mathrm{r}}^{\mathrm{g}} p_{\mathrm{r}}^{\mathrm{g}}}{l_{\mathrm{r}}} = \frac{\rho g_{\mathrm{r}}}{l_{\mathrm{r}}} \quad (11b)$$

Finally, the scale factors derived from all the governing and state equations, including liquid-gas migration, heat transfer and mechanical deformation, can be consolidated and presented in Table 1.

Table 1. Scale factors for all parameters of THM processes in unsaturated soils.

Parameters	Symbol	Model/Prototype	Parameters	Symbol	Model/Prototype
Length	l	$1/N$	Intrinsic / relative permeability	K, k_{r}	1
Gravity acceleration	g	N	Diffusion coefficient	D_{a}	1
Time	t	N^2	Velocity	v	N
Stress	σ, σ'	1	Viscosity	μ	1
Strain	ε	1	Pore pressure	p	1
Density	ρ	1	Thermal conductivity	K_T	1
Elasticity	E	1	Temperature	T	1
Porosity	φ	1	Thermal expansion coefficient	β	1
Saturation	S	1	Specific heat capacity	C	1

2.2.2 Boundary conditions

Boundary conditions play a crucial role in obtaining a well-defined solution to a specific problem. The three most common types of boundary conditions are Dirichlet, Neumann, and Robin conditions. The Dirichlet and Neumann conditions in both the centrifugal model and the prototype are:

$$X_{\mathrm{m}} = X_{\Gamma\mathrm{m}} \ \text{ on } \ \Gamma_{X\mathrm{m}}^{\mathrm{D}} \quad (12a)$$

$$X_{\mathrm{p}} = X_{\Gamma\mathrm{p}} \ \text{ on } \ \Gamma_{X\mathrm{p}}^{\mathrm{D}} \quad (12b)$$

$$\mathbf{J}_{X\mathrm{m}} \cdot \mathbf{n} = q_{\Gamma\mathrm{m}}^{\mathrm{N}} \ \text{ on } \ \Gamma_{X\mathrm{m}}^{\mathrm{N}} \quad (12c)$$

$$\mathbf{J}_{X\mathrm{p}}\cdot\mathbf{n} = q_{\Gamma\mathrm{p}}^{\mathrm{N}} \text{ on } \Gamma_{X\mathrm{p}}^{\mathrm{N}} \tag{12d}$$

where X = the primary variable, such as pore liquid / gas pressure or temperature, X_Γ = the value of X in the Dirichlet boundary Γ_X^{D}, $\mathbf{J}_{X\mathrm{m}}$ = flux for water / air migration or heat transfer, $\mathbf{n}$ = unit normal vector, and q_Γ^{N} = the flux normal to the Neumann boundary.

According to previous derivation, we have:

$$X_{\Gamma\mathrm{r}} = \frac{X_{\Gamma\mathrm{m}}}{X_{\Gamma\mathrm{p}}} = 1 \tag{13a}$$

$$q_{\Gamma\mathrm{r}}^{\mathrm{N}} = \frac{q_{\Gamma\mathrm{m}}^{\mathrm{N}}}{q_{\Gamma\mathrm{p}}^{\mathrm{N}}} = N \tag{13b}$$

where $X_{\Gamma\mathrm{r}}$ = scale factor for the value of primary variable in the Dirichlet boundary, and $q_{\Gamma\mathrm{r}}^{\mathrm{N}}$ = scale factor for the flux normal to Neumann boundary.

Therefore, the similarity of the THM coupled problem in unsaturated soils for the centrifugal model aligns with the requirement to accurately reflect the prototype when utilizing the parametric scale factors outlined in Table 1, and adhering to the corresponding conditions specified by Eq. 13(a) or 13(b). In the cases of Robin conditions, which represent a linear combination of Dirichlet and Neumann conditions, a detailed discussion is deemed unnecessary.

3. Numerical software and verification

To explore the THM responses and the similarity of hypergravity tests in unsaturated soils, a THM coupled model is adopted in this study based on OpenGeoSys [13]. The implementation of the coupled model follows a monolithic method known for its higher precision and improved convergency. Additionally, we employed the Backward Euler scheme for time discretization. Non-linear iteration was addressed using the Newton-Raphson method, with the approximate analytical Jacobian derived to handle the complexities of the coupled problem. Similar to the THM model for saturated soils, the gravity effect is incorporated into the unsaturated THM model by introducing gravity-related terms into the governing equations. Subsequently, pre-calculation for initial values of pore pressures and stresses, and post-calculation for targeted cases, are conducted.

To verify the THM model in unsaturated soils. Schrefler et al. [15] conducted a numerical example involving one-dimensional THM coupled responses using the Comes-Geo code. Figure. 2 depicts the mesh division and boundary conditions for this case. The dimensions are given with a height (H) of 0.1 m and a width ($0.1H$) of 0.01 m, where the lateral and bottom boundaries are insulated, impermeable and simply supported. Initial values for temperature (T_0), gas pressure (p_{G0}), and liquid pressure (p_{L0}) are 283.15 K, 102 kPa and -420 kPa respectively. To simulate environmental changes, a temperature increment, noted as $\triangle T$, of 15 K and a liquid pressure decrement, marked as $\triangle p_{\mathrm{L}}$, of 140 kPa are applied to the top boundary. The soil water retention curve is modelled using the Brooks-Corey model, and

the gas/liquid relative permeability is described by the van Genuchten model. These choices align with existing studies [4, 13, 15].

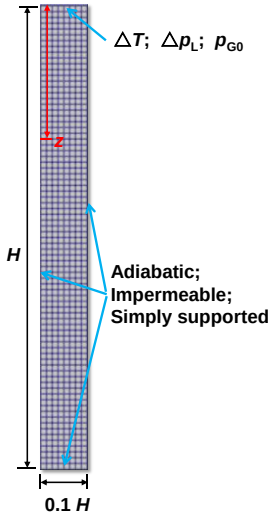

Figure. 2. Mesh division and boundary conditions of the verification model

Figure 3 illustrates the THM coupled responses in unsaturated soils, presenting a comparison with findings from previous studies [4, 13, 15]. As is shown in Figure. 3(a), temperature profiles at different times along the normalized depth show favourable agreement among Schrefler et al. [15], Zhu et al. (2020) using OGS-5 [4], and the present model implemented in OGS-6 [13]. Figures 3(b) and 3(c) demonstrate generally consistent liquid saturation and vertical displacement. Slight differences in liquid saturation between this study and Zhu et al. [4] may arise from considerations of solid and water compressibility in OGS-5. Additionally, the marginal disparities in liquid saturation and vertical displacement compared to Schrefler et al. [15] could be attributed to the temperature-dependent model for soil water retention curve applied in their simulation, along with different spatial and temporal discretization methods. Consequently, this model in OGS-6 exhibits effectiveness in simulating THM coupled behavior in unsaturated soils, as evidenced by its alignment with existing research.

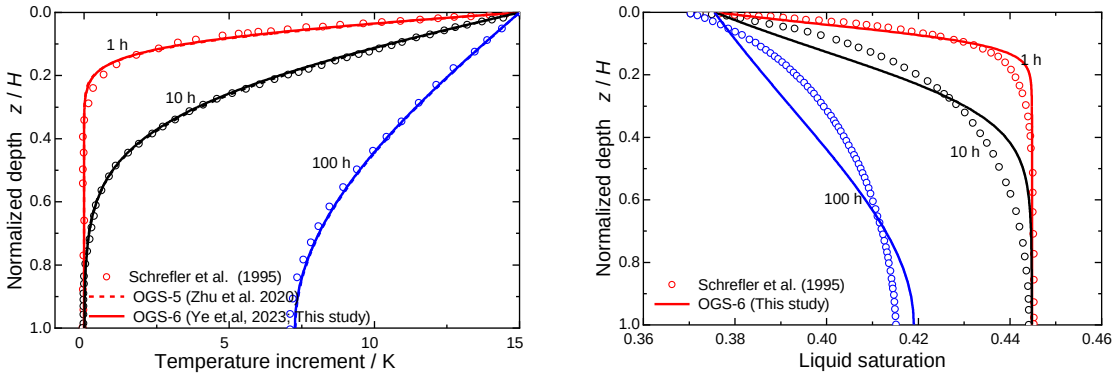

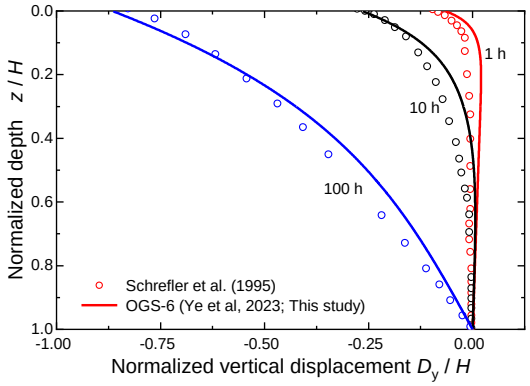

Figure. 3. THM coupled responses in unsaturated soils compared to existing researches: (a) temperature increment; (b) liquid saturation; (c) vertical displacement.

4. Numerical simulation

As depicted in Figure 4, marine sediments or coastal areas commonly exist in an unsaturated state, experiencing variations in temperature and pore pressure. In the prototype, the depth is denoted as *H*, and under the influence of gravity, both liquid pressure and effective stresses increase along the depth. Conducting in-situ tests for such conditions is often associated with high costs and extended durations. Therefore, indoor centrifugal models emerge as an effective alternative, capable of capturing both pore pressure and effective stress distributions. To investigate the similarity between the prototype and centrifugal model, a comparative analysis is undertaken between the 1g numerical model for the prototype and the *N*g numerical model for the centrifugal model in this segment.

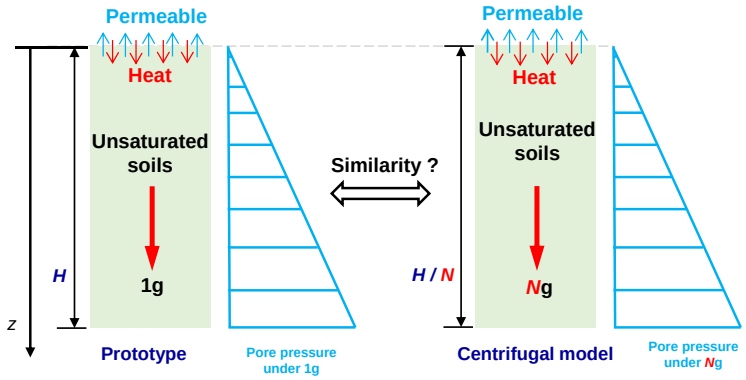

Figure. 4. Diagram for the similarity between prototype and centrifugal model.

4.1 Similarity of boundary condition

As per the earlier derivation, the satisfaction of similarity between the prototype and centrifugal model hinges on the provision of scaling factors for the parameters outlined in Table 1. Despite this, the previous equations have not undergone numerical verification or been explicitly linked to the boundary conditions. Hence, further investigation is warranted

to validate and establish the numerical connections between the derived equations and the boundary conditions.

4.1.1 Dirichlet condition

The Dirichlet condition is a prevalent boundary condition in practical applications. To delve into the similarity between the prototype and the numerical model, a *N*g numerical model with a depth of *H*/*N* has been implemented for comparison with the previous model.

Figure 5 presents profiles of temperature increment, gas pressure, liquid pressure, and liquid saturation at different times. Notably, there is almost no discernible difference between the 1g and *N*g models for all variables, affirming the accuracy of the derived equations and demonstrating the similarity between the prototype and the numerical model under Dirichlet conditions. In Figure 5(a), temperature gradually increases from near the top boundary to the further boundary, with a higher gradient near the top boundary. Figure 5(b) illustrates that liquid pressure at the lower region linearly increases along the depth due to gravity for a short period, propagating from near to far over time. In contrast, Figure 5(c) shows that the effects of gravity on gas pressure are not apparent, and a local decline occurs near the top boundary and gradually extends to the further region. This can be attributed to several factors: (1) the gas phase is more sensitive to temperature variations, leading to gas expansion; (2) constant gas pressure applied to the top boundary allows the gas phase to pass through; (3) gas phase moves much faster than the liquid phase due to its significantly lower viscosity. Interestingly, the trend of liquid saturation in Figure 5(d) corresponds to that of liquid pressure, given the larger variation in liquid pressure compared to gas pressure.

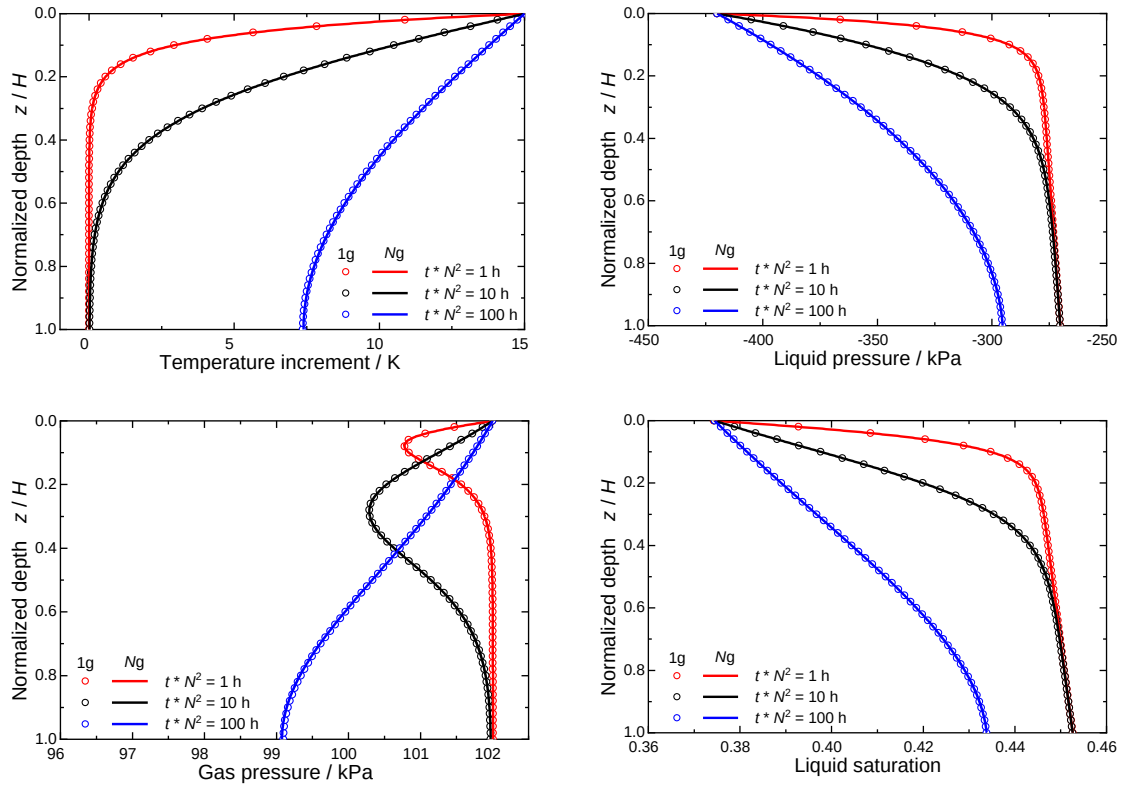

Figure. 5. Comparison between 1g and *N*g model with Dirichlet condition: (a) temperature increment; (b) liquid pressure; (c) gas pressure; (d) liquid saturation.

4.1.2 Neumann condition

The Neumann condition is another frequently encountered boundary condition. To investigate the similarity between the prototype and the numerical model, *N*g numerical models are employed, with scaling values based on scaling laws, as well as with the same values used in the 1g model (referred to as *N*g-IniC).

Figure 6 presents profiles of temperature increment, gas pressure, liquid pressure, and liquid saturation at different times for the three mentioned cases under Neumann conditions. Notably, all variables exhibit no difference between the 1g and *N*g models, affirming the correctness of the established similarity for Neumann conditions. However, significant discrepancies between the *N*g and *N*g-IniC models are apparent for temperature and gas pressure, especially over a prolonged duration. This suggests that special attention is warranted when considering the Neumann boundary for investigating the similarity between the prototype and centrifugal model. In Figure 6(a), temperature exhibits a faster increase over time when a fixed Neumann condition is applied to the energy conservation equation. Generally, it appears that liquid pressure is scarcely affected by different Neumann conditions in Figure 6(b), except for a minor deviation at time 100 h. In Figure 6(c), the discrepancy in local gas pressure decline is magnified over time in the *N*g-IniC model. This is attributed to the heightened sensitivity of gas phase to temperature variations. For liquid saturation in Figure 6(d), a similar trend compared to liquid pressure is still noticeable.

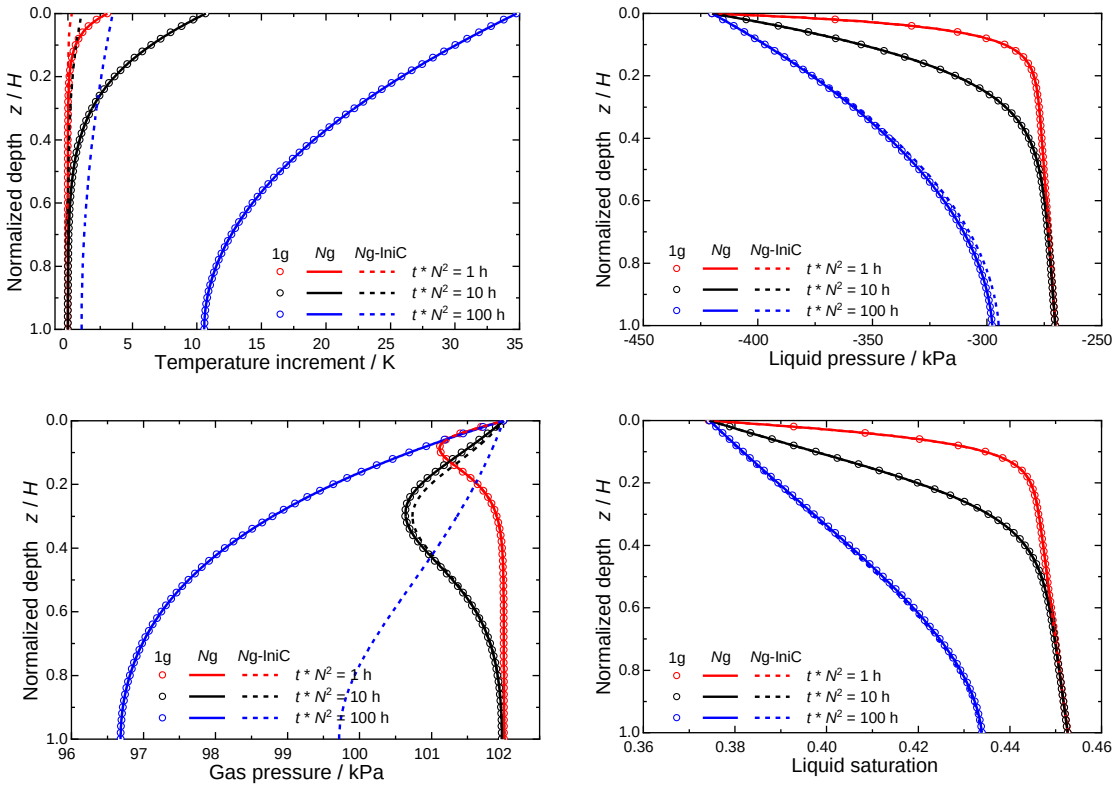

Figure. 6. Comparison between 1g and *N*g model with Neumann condition: (a) temperature increment; (b) liquid pressure; (c) gas pressure; (d) liquid saturation.

4.2 Parametric analysis

Previous analyses primarily focus on the similarity between the prototype and centrifugal model under Dirichlet or Neumann boundaries, with an emphasis on the coupled behavior concerning temperature and gas pressure due to the perceived lesser impact of temperature on liquid pressure/saturation. However, it's crucial to recognize that liquid pressure and saturation can also be significantly influenced by temperature and gas pressure. A detailed investigation is required to explore various conditions and types of soils in this context.

4.2.1 Boundary temperature increment

In practical scenarios, environmental temperatures undergo variations due to day-night or seasonal cycling. Consequently, the following discussion explores three cases with temperature changes ΔT = 15, 30, 45 K to simulate such environmental fluctuations.

Figure 7 illustrates the effects of ΔT on profiles of field variables at different times. Notably, all variables exhibit significant differences, indicating that both liquid pressure and saturation can be influenced by the coupled behavior. In Figure 7(a), the evolution tendency appears similar at different boundary temperatures. Figure 7(b) shows that the local decline of liquid pressure propagates from near to far over time, with the amplitude amplifying. The value of the maximum variation at 100 h is about -12 kPa. Similarly, in Figure 7(c), the amplitude of the local decline of gas pressure is noticeable, and the amplitude at different times shows a slight increase over time. For liquid saturation in Figure 7(d), a local increase is observed, progressing further over time, indicating phase transition between water vapor and liquid water. From the previous illustration, it can be concluded that gas pressure is more sensitive to temperature variation than liquid pressure, leading to pore pressure differences and consequent variations in saturation. The change in saturation means the occurrence of phase transition between liquid and gas phase.

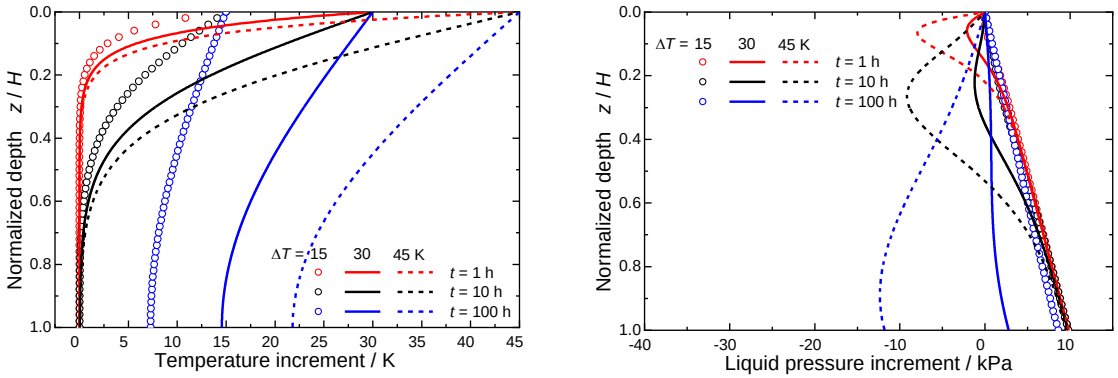

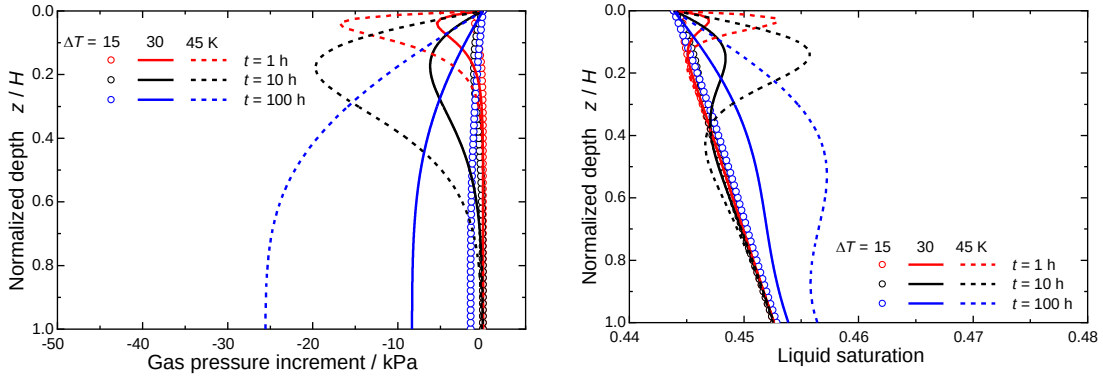

Figure. 7. Comparison among different boundary temperature increment: (a) temperature increment; (b) liquid pressure increment; (c) gas pressure increment; (d) liquid saturation.

4.2.2 Initial pore pressure

The initial pore liquid/gas pressure can vary significantly under different conditions. In coastal areas, gas pressure typically remains close to atmospheric pressure, and negative liquid pressure may occur, as seen in the previous example. In unsaturated marine sediments, such as those with a free gas layer under gas hydrate-bearing sediments, pore pressure is usually much higher than atmospheric pressure. Therefore, the following discussion explores three cases with increments of pore pressure Δp = 0, 500, 1000 kPa.

Figure 8 illustrates the effects of Δp on profiles of field variables at different times. Both liquid and gas pressures exhibit slight differences at different initial pore pressures. In Figure 8(a), the tendency of a linear rise along the depth due to gravity is still present, with only a minor difference noticed in all the profiles. Similarly, in Figure 8(b), the amplitude of variation for gas pressure with different Δp is within 5 kPa. In summary, it can be concluded that the THM coupled behavior in unsaturated soils shows slight deviations with Δp. The reason is that the same increase in Δp for both liquid and gas pressure means the capillary pressure remains unchanged, resulting in the same initial saturation. Consequently, liquid-gas migration under higher pore pressure is almost the same as that under lower pore pressure. Any slight difference is likely caused by variations in pressure-dependent gas density, molar mass, and related terms in the governing/state equations.

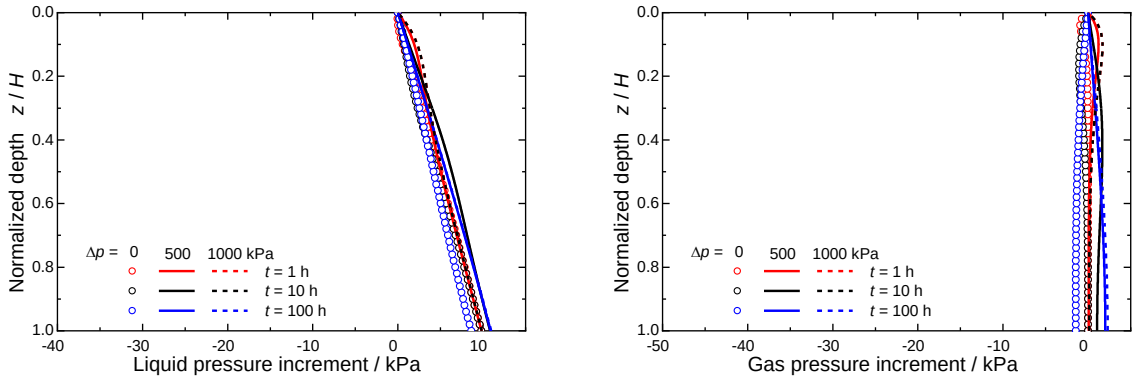

Figure. 8. Comparison among different initial pore pressure: (a) liquid pressure increment; (b) gas pressure increment.

4.2.3 Gas diffusion coefficient

From the previous illustration, it is evident that gas phase is more sensitive to temperature variation than liquid phase. In the context of gas phase, diffusive flux plays a crucial role in liquid-gas migration. The reported gas diffusion coefficient in free air is approximately 10^{-6} to 10^{-5} m^2/s, which is greatly reduced by several orders of magnitude in unsaturated soils [16]. Therefore, three cases with gas diffusion coefficient D_a = 1.25×10^{-8}, 1.25×10^{-7}, 1.25×10^{-6} m^2/s are discussed in the following.

Figure 9 illustrates the effects of D_a on profiles of field variables at different times. Both liquid and gas pressures exhibit significant difference with varying D_a. In Figure 9(a), the amplitude of liquid pressure variation increases with D_a, and the peak value is also advanced. Similarly, in Figure 9(b), the amplitude of gas pressure variation is amplified with Da, and the maximum variation even approaches about 45 kPa at 100 h. In summary, it can be concluded that the THM coupled behavior in unsaturated soils is highly associated with D_a. This is attributed to the fact that both advective and diffusive fluxes play crucial roles in liquid-gas migration in unsaturated soils, particularly for low permeability conditions.

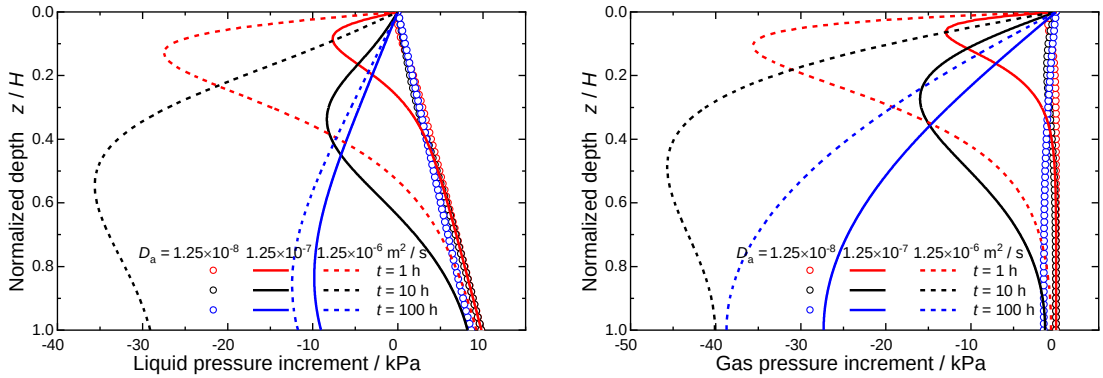

Figure. 9. Comparison among different gas diffusion coefficient: (a) liquid pressure increment; (b) gas pressure increment.

4.2.4 Air entry pressure

In coastal or marine sediments, the soils vary from sand to clay. Air entry pressure is a key parameter of the SWRC in unsaturated state and highly associated with types of soils. Thus, three cases with air entry pressure changes p_0 = 200, 288, 376 K are discussed as follows.

Figure. 10 illustrates the effects of p_0 on profiles of field variables at different time. It can be noticed that all the variables exhibit great difference with different p_0. In Figure. 10(a), a noticeable discrepancy for temperature increment occurs, behaving a delay of the evolution with high p_0. As is depicted in Figure. 10(b), large local decline of liquid pressure also happens with high p_0. The amplitude has been amplified to about -15 kPa at 1 h and 10 h when p_0 = 376 kPa, whereas liquid pressure tends to be dissipating at 100 h. In Figure. 10(c), the amplitude of the local decline of gas pressure can also be noticed and the amplitude of at different time shows a slight rise over time. This means that the gas migration is much slower than that of liquid phase. For liquid saturation in Figure. 10(d), different initial value and variation can be both observed. A higher p_0 is associated with a larger liquid saturation due to the difficulty for air entry into the sediments with small soil particles. We can even notice

the initial full liquid saturated when p_0 = 376 kPa, and gas phase gradually appears caused by liquid water evaporation and then disappears induced by water vapor condensation. From these illustrations, it can be concluded that air entry pressure is highly associated with the THM coupled behavior in unsaturated soils, and it should be precisely determined in practice.

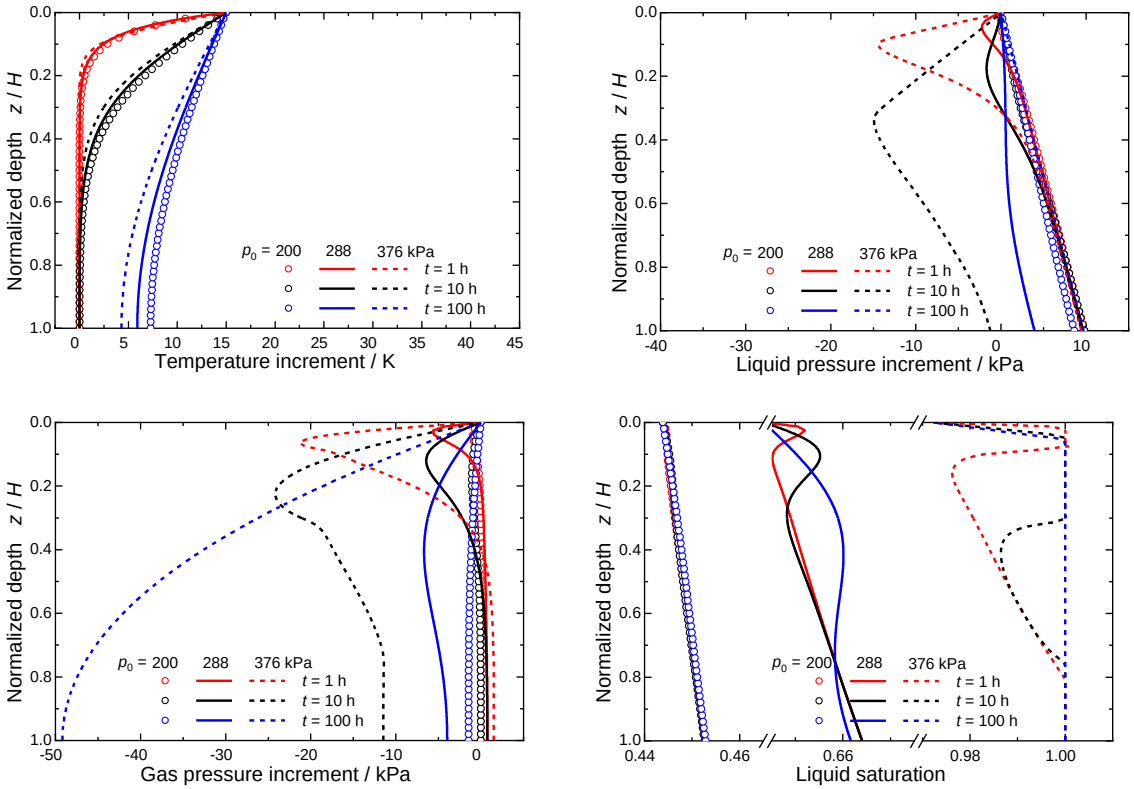

Figure. 10. Comparison among different gas entrance pressure coefficient: (a) temperature increment; (b) gas pressure increment; (c) liquid pressure increment; (d) liquid saturation.

5. Conclusions

This paper presents an assessment of THM coupled behavior in unsaturated soils, incorporating the influence of gravity through both theoretical and numerical methods. The main conclusions are outlined as follows:

(1) The similarity for THM coupled centrifugal tests in unsaturated soils has been derived based on the analysis of governing equations and scaling laws, encompassing mass balance, energy conservation, and linear momentum equations. A comprehensive analysis is proposed, considering boundary conditions.

(2) Verification of the similarity between the prototype and the centrifugal model has been achieved through numerical models under 1g and Ng conditions, utilizing a THM coupled model with the OpenGeoSys FEM code. Discussions on Dirichlet and Neumann conditions reveal that careful treatment is required for the Neumann condition flux in the *N*g model.

(3) Numerical simulations indicate that both gas and liquid pressures are influenced by

temperature variation, leading to phase transitions between liquid water and water vapor. Pore pressure difference, rather than initial pore pressure, significantly impacts thermo-hydro-mechanical responses in unsaturated soils, offering insights for reflecting deep marine sediments without precise pore pressure restoration.

(4) Gas diffusion coefficient, crucial for low permeability conditions, plays a key role as diffusive flux cannot be neglected in comparison to advective flux in liquid-gas migration. Air entry pressure, linked to soil types, is another vital parameter. Higher air entry pressure implies slower liquid-gas migration, causing delays in heat transfer, increased pore pressure variation amplitude, elevated initial liquid saturation, and noticeable phase transitions.

Acknowledgments: The first author is grateful to all the members of the OpenGeoSys team at Helmholtz Centre for Environmental Research (UFZ), especially Prof. Olaf Kolditz, Dr. Haibing Shao, Prof. Thomas Nagel, Dr. Renchao Lu and Dr. Boyan Meng for supporting his research stay in Germany.

Funding: This research was funded by China Scholarship Council (No. 202106320166) and National Natural Science Foundation of China (No. 51988101).

Conflict of interest: The authors declare that they have no known competing financial interests or personal relationships that could have appeared to influence the work reported in this paper.

References:

1. Li JF, Ye JL, Qin XW *et al*. The first offshore natural gas hydrate production test in South China Sea. China geology. 2018, 1(1):5-16. Doi: 10.31035/cg2018003
2. Ye ZG, Wang LJ, Zhu B, *et al*. A thermo-hydro-chemo-mechanical coupled model for natural gas hydrate-bearing sediments considering gravity effect. Journal of Natural Gas Science and Engineering. 2022, 108:104823. Doi: 10.1016/j.jngse.2022.104823
3. Xu C, Yu B, Zhang Z, *et al*. Numerical simulation of a buried hot crude oil pipeline during shutdown. Petroleum Science. 2010, 7:73-82. Doi: 10.1007/s12182-010-0008-x
4. Zhu B, Ye ZG, Wang LJ, *et al*. Hydro-mechanical behavior of unsaturated soil surrounding a heated pipeline considering moisture evaporation and condensation. Computers and Geotechnics. 2020, 119:103377. Doi: 10.1016/j.compgeo.2019.103377
5. Laloui L, Nuth M, Vulliet L. Experimental and numerical investigations of the behaviour of a heat exchanger pile. International Journal for Numerical and Analytical Methods in Geomechanics. 2006, 30(8): 763-781. Doi: 10.1002/nag.499
6. Liu H, Cai Y, Zhong Y, *et al*. Thermo-hydro-mechanical response of a multi-layered pavement with imperfect interface based on dual variable and position method. Applied Mathematical Modelling. 2021, 99: 704-729. Doi: 10.1016/j.apm.2021.07.001
7. Yavari N, Tang AM, Pereira JM, *et al*. Mechanical behaviour of a small-scale energy pile in saturated clay. Géotechnique. 2016, 66(11):878-87. Doi: 10.1680/jgeot.15.T.026
8. Ng CWW, Shi C, Gunawan A, *et al*. Centrifuge modelling of energy piles subjected to

heating and cooling cycles in clay. Géotechnique letters, 2014. 4(4), 310-316. Doi:10.1680/geolett.14.00063

9. Schofield AN. Cambridge geotechnical centrifuge operations. Géotechnique. 1980, 30(3): 227-268. Doi: 10.1680/geot.1980.30.3.227
10. Nahavandi AN, Castellana FS, Moradkhanian EN. Scaling laws for modeling nuclear reactor systems. Nuclear Science and Engineering. 1979, 72(1):75-83. Doi: 10.13182/NSE79-A19310
11. Stewart MA, McCartney JS. Centrifuge modeling of soil-structure interaction in energy foundations. Journal of Geotechnical and Geoenvironmental Engineering. 2014, 140(4): 04013044. Doi: 10.1061/(ASCE)GT.1943-5606.0001061
12. Bilke L, Flemisch B, Kalbacher T, *et al*. Development of open-source porous media simulators: principles and experiences. Transport in Porous Media. 2019, 130:337-361. Doi: 10.1007/s11242-019-01310-1
13. Ye ZG, Wang LJ, Zhu B, *et al*. A model on assessing effects of gas diffusion in multifield coupled process for unsaturated soils. Environmental Earth Sciences. 2023, 82:180. Doi: 10.1007/s12665-023-10836-z
14. Sanavia L, Pesavento F, Schrefler BA. Finite element analysis of non-isothermal multiphase geomaterials with application to strain localization simulation. Computational Mechanics. 2006, 37: 331-348. Doi: 10.1007/s00466-005-0673-6
15. Schrefler BA., Zhan X, Simoni L. A coupled model for water flow, airflow and heat flow in deformable porous media. International Journal of Numerical Methods for Heat and Fluid Flow. 1995, 5(6), 531-547. Doi: 10.1108/EUM0000000004077
16. Resurreccion A C., Moldrup P, Kawamoto K, *et al*. Hierarchical, bimodal model for gas diffusivity in aggregated, unsaturated soils. Soil Science Society of America Journal. 2010, 74(2), 481-491. Doi: 10.2136/vzj2011.0065